

# Phase transition during inflation and the gravitational wave signal at pulsar timing arrays

Haipeng An,<sup>1,2,3,4,\*</sup> Boye Su,<sup>1,†</sup> Hanwen Tai,<sup>5,6,‡</sup> Lian-Tao Wang,<sup>5,6,7,§</sup> and Chen Yang<sup>1,¶</sup>

<sup>1</sup>*Department of Physics, Tsinghua University, Beijing 100084, China*

<sup>2</sup>*Center for High Energy Physics, Tsinghua University, Beijing 100084, China*

<sup>3</sup>*Center for High Energy Physics, Peking University, Beijing 100871, China*

<sup>4</sup>*Frontier Science Center for Quantum Information, Beijing 100084, China*

<sup>5</sup>*Department of Physics, The University of Chicago, Chicago, IL 60637, USA*

<sup>6</sup>*Enrico Fermi Institute, University of Chicago, Chicago, IL 60637, USA*

<sup>7</sup>*Kavli Institute for Cosmological Physics, University of Chicago, Chicago, IL 60637, USA*

Gravitational wave signal offers a promising window into the dynamics of the early universe. The recent results from pulsar timing arrays (PTAs) could be the first glimpse of such new physics. In particular, they could point to new details during the inflation, which can not be probed by other means. We explore the possibility that the new results could come from the secondary gravitational wave sourced by curvature perturbations, generated by a first-order phase transition during the inflation. Based on the results of a field-theoretic lattice simulation of the phase transition process, we show that the gravitational wave signal generated through this mechanism can account for the new results from the PTAs. We analyze the spectral shape of the signal in detail. Future observations can use such information to distinguish the gravitational wave signal considered here from other possible sources.

## INTRODUCTION

Despite the enormous progress in our knowledge about the early universe, large gaps still remain. Gravitational wave (GW) signal offers a new window into the early universe epochs and dynamics that can't be probed by other means. PTA collaborations have recently released further evidence that the common-spectrum process observed previously has the Hellings-Downs angular correlation [1–7]. This indicates the existence of a gravitational wave (GW) background in the nano-Hz frequency range [8].

GW signal in this frequency range can be produced by low-scale phase transitions in the radiation domination (RD) era [9–27], supermassive black hole mergers [28–36], and topological defects, such as cosmic strings and domain walls [23, 37–51]. At the same time, such a signal can be generated during the inflation, approximately 15 e-fold after the CMB mode exit the horizon. Various possible mechanisms have been studied [52–73]. New physics scenarios during the inflation as a possible origin for the observed signal have been proposed [74–79]. In the work, we focus on the possibility of the source being a first-order phase transition during inflation [80–82]. The bubble collision process during the phase transition can produce GWs. Such so-called primary GW signal is suppressed by  $(H_{\text{inf}}/\beta)^5$  and  $(L/\rho_{\text{inf}})^2$ , where  $H_{\text{inf}}$  is the Hubble expansion rate,  $\beta$  is the phase transition rate,  $L$  is the latent heat density and  $\rho_{\text{inf}}$  is the total energy density of the universe during inflation. At the same time, the phase transition process is also a source of curvature perturbation. Such curvature perturbation, after inflation, can generate the so-called secondary GWs [83], see also [84, 85]. Compared to the primary GWs, the sec-

ondary GWs can be naturally enhanced by the slow-roll parameter and thus can give rise to the signal observed by the PTAs.

In this work, we perform a field-theoretic simulation of the bubble nucleation and collision process, with a lattice of size  $1000 \times 1000 \times 1000$ , to calculate induced curvature perturbation. Based on these results, we can predict both the strength and the spectral shape of the secondary GW signal. In the absence of a combination of the data sets from different PTAs, we choose the results from the NANOGrav collaboration [1] as a benchmark for comparison. We show that both the size and the shape of the observed signal by NANOGrav [1, 5] in the region with the frequency  $f < (1 \text{ year})^{-1}$  can be well fit by the secondary GWs produced by first-order phase transition produced during inflation.

## THE MODEL

In this work, we model a spectator sector with a single real scalar field,  $\sigma$ . The Lagrangian of  $\phi$  and  $\sigma$  is

$$\mathcal{L} = -\frac{1}{2}g^{\mu\nu}\partial_\mu\phi\partial_\nu\phi - \frac{1}{2}g^{\mu\nu}\partial_\mu\sigma\partial_\nu\sigma - V(\phi, \sigma). \quad (1)$$

For the convenience of later discussions, we decompose  $V(\phi, \sigma)$  as

$$V(\phi, \sigma) = V_0(\phi) + V_1(\phi, \sigma), \quad (2)$$

where  $V_0(\phi) = V(\phi, 0)$ .

The inflaton field  $\phi$  can be decomposed as  $\phi_0 + \delta\phi$ , where  $\phi_0$  is the homogeneous part, and  $\delta\phi$  is the perturbation. The crucial part in the Lagrangian (1) is that

the mass of the  $\sigma$  field is  $\phi_0$  dependent, with

$$m_\sigma^2 = (c_m \phi_0^2 - m^2). \quad (3)$$

In this scenario, the evolution of  $\phi_0$  will change the shape of the potential and thus trigger a first-order phase transition. The general framework for such a scenario can be found in [81, 82]. The details of the specific model used in the numerical simulation in this work are presented in the appendix. The time scale of the phase transition is determined by  $t \sim \beta^{-1}$ ,  $\beta = -dS_4/dt$ , where  $S_4$  is the bounce action between the false and true vacuums, and  $t$  is the physical time. The value of  $\beta$  depends on the details of the models in the inflaton and spectator sectors. For the class of models considered here,  $\beta/H_{\text{inf}} \sim \mathcal{O}(10)$  [81, 82],  $H_{\text{inf}}$  is the Hubble parameter during inflation.  $\beta^{-1}$  is the typical size of the bubbles.

Through this work, we use the Newtonian gauge, and thus the metric perturbation can be written as

$$g_{00} = -a^2(1 + 2\Phi), g_{0i} = 0, g_{ij} = a^2[\delta_{ij}(1 - 2\Psi) + h_{ij}], \quad (4)$$

and during inflation, we have  $a = -1/H_{\text{inf}}\tau$  with  $\tau$  the conformal time. In radiation domination, we have  $a = a_R^2 H_R \tau$ , where  $a_R$  and  $H_R$  are the scale factor and the Hubble parameter at reheating. In this work, we assume de Sitter inflation with instantaneous reheating. Therefore, we have  $H_R = H_{\text{inf}}$ .

## PRIMARY AND SECONDARY GWS

In our setup, there are two periods that classical GWs can be copiously produced. In both cases, the GWs satisfy the differential equation,

$$h_{ij}^{\text{TT}''} + 2\mathcal{H}h_{ij}^{\text{TT}'} - \nabla^2 h_{ij}^{\text{TT}} = 16\pi G\mathcal{T}_{ij}, \quad (5)$$

where ‘‘TT’’ denotes the transverse and traceless components,  $\mathcal{H} = a'/a$ , and  $\mathcal{T}_{ij}$  is the source of GWs.

During inflation, the main contribution to the GWs is from the TT components of the energy-momentum tensor. The energy-momentum tensor is composed of  $\sigma$  and  $\delta\phi$ , where  $\delta\phi$  is induced by the back reaction from the phase transition as discussed later. We call both of these contributions primary GWs. After being produced, the primary GWs will exit the horizon, and their field strength will be frozen to fixed values. The primary GWs will oscillate again once they reenter the horizon.

In addition to the primary GWs, the phase transition will also induce scalar curvature perturbation leading to secondary GWs after inflation. In particular, with the Newtonian gauge in Eq. (4), the source  $\mathcal{T}_{ij}$  is composed of terms quadratic in  $\Phi$  [83, 84].

In summary, the source term can be written as

$$\mathcal{T}_{ij} = \begin{cases} [\partial_i \sigma \partial_j \sigma + \partial_i \delta\phi \partial_j \delta\phi]^{\text{TT}}, & \text{primary} \\ -M_{\text{pl}}^2 \left[ 4\Phi \partial_i \partial_j \Phi + 2\partial_i \Phi \partial_j \Phi - \frac{2}{\mathcal{H}^2 - \mathcal{H}'} \partial_i (\Phi' + \mathcal{H}\Phi) \partial_j (\Phi' + \mathcal{H}\Phi) \right]^{\text{TT}}, & \text{secondary} \end{cases} \quad (6)$$

## GENERATION OF THE CURVATURE PERTURBATION

From the Lagrangian (1), we can derive the equation of motion for the Fourier modes of the inflaton perturbation,

$$\delta\tilde{\phi}_{\mathbf{q}}'' - \frac{2}{\tau}\delta\tilde{\phi}_{\mathbf{q}}' + \left( q^2 + \frac{1}{H_{\text{inf}}^2 \tau^2} \frac{\partial^2 V_0}{\partial \phi_0^2} \right) \delta\tilde{\phi}_{\mathbf{q}} = \mathcal{S}_{\mathbf{q}}, \quad (7)$$

where the source  $\mathcal{S}_{\mathbf{q}}$  is

$$\mathcal{S}_{\mathbf{q}} = -\frac{1}{H_{\text{inf}}^2 \tau^2} \left[ \frac{\partial V_1}{\partial \phi} \right]_{\mathbf{q}} - \left\{ \frac{2\tilde{\Phi}_{\mathbf{q}}}{H_{\text{inf}}^2 \tau^2} \left( \frac{\partial V_0}{\partial \phi_0} + \left[ \frac{\partial V_1}{\partial \phi} \right]_0 \right) + \frac{\dot{\phi}_0}{H_{\text{inf}} \tau} \left( 3\tilde{\Psi}'_{\mathbf{q}} + \tilde{\Phi}'_{\mathbf{q}} \right) \right\}. \quad (8)$$

Here the symbol  $[\dots]_{\mathbf{q}}$  denotes the Fourier mode with comoving momentum  $\mathbf{q}$ , and  $\dot{\phi}_0$  denotes  $d\phi_0/dt$ . There are two source terms on the right-hand side of Eq. (7), in

which the first term is from the direct interaction between  $\phi$  and  $\sigma$ , whereas the second term is purely gravitational. In the case of polynomial interaction  $c_m \phi^2 \sigma^2$ , we have

$$\left[ \frac{\partial V_1}{\partial \phi} \right]_{\mathbf{q}} = c_m [\phi \sigma^2]_{\mathbf{q}} \approx c_m \phi_0 [\sigma^2]_{\mathbf{q}}. \quad (9)$$

Due to the Einstein equations,  $\Phi$  and  $\Psi$  satisfy the differential equation

$$\tilde{\Psi}'_{\mathbf{q}} - \frac{\tilde{\Phi}_{\mathbf{q}}}{\tau} = -4\pi G_N \left( \frac{\dot{\phi}_0 \delta\tilde{\phi}_{\mathbf{q}}}{H_{\text{inf}} \tau} + \left[ \frac{\partial_i}{\partial^2} (\sigma' \partial_i \sigma) \right]_{\mathbf{q}} \right). \quad (10)$$

From the energy-momentum conservation, we have

$$\tilde{\Phi}_{\mathbf{q}} - \tilde{\Psi}_{\mathbf{q}} = -8\pi G_N \tilde{\pi}_{\mathbf{q}}^S / (H_{\text{inf}}^2 \tau^2), \quad (11)$$

where  $\pi^S$  is the anisotropic inertia

$$\tilde{\pi}_{\mathbf{q}}^S = -\frac{3}{2} H_{\text{inf}}^2 \tau^2 q_i q_j q^{-4} [(\partial_i \sigma \partial_j \sigma)^{\text{TL}}]_{\mathbf{q}}, \quad (12)$$

where the upper script TL refers to the traceless part.

During slow-roll inflation, the *mass term*,  $\partial^2 V_0 / \partial \phi_0^2$ , in the Eq. (7) is negligible. The solution of  $\delta \tilde{\phi}_{\mathbf{q}}$  can be written as

$$\delta \tilde{\phi}_{\mathbf{q}}(\tau) = \int_{-\infty}^{\tau} d\tau' \tilde{G}(\tau, \tau', q) \mathcal{S}_{\mathbf{q}}(\tau'), \quad (13)$$

where the Green's function

$$\begin{aligned} \tilde{G}(\tau, \tau'; q) &= -\frac{1}{q^2 \tau'^2} (\tau - \tau') \cos q(\tau - \tau') \\ &\quad + \frac{1}{q^3 \tau'^2} [(1 + q^2 \tau \tau') \sin q(\tau - \tau')]. \end{aligned} \quad (14)$$

After the phase transition, the universe returns to single-field inflation. Thus, the gauge-invariant quantity,

$$\zeta_{\mathbf{q}} = -\tilde{\Psi}_{\mathbf{q}} - \frac{H_{\text{inf}} \delta \tilde{\phi}_{\mathbf{q}}}{\dot{\phi}_0}, \quad (15)$$

is conserved when evolving outside of the horizon.

Several e-folds after the phase transition, the  $\Phi$  contribution to  $\zeta$  becomes negligible since its direct source from the  $\sigma$  field quickly redshifts away. Hence, we have

$$\zeta_{\mathbf{q}} = -\frac{H_{\text{inf}}}{\dot{\phi}_0 q} \int_{-\infty}^0 d\tau' \mathcal{K}(q\tau') \mathcal{S}_{\mathbf{q}}(\tau'), \quad (16)$$

where the integral kernel is

$$\mathcal{K}(\eta) = \frac{1}{\eta} \left( \cos \eta - \frac{\sin \eta}{\eta} \right). \quad (17)$$

## THE SIGNAL

In this work, we use a  $1000 \times 1000 \times 1000$  lattice to simulate the phase transition process in de Sitter space and numerically solve Eqs. (7), (10) and (11) to calculate the various contributions to  $\zeta_{\mathbf{q}}$ . The details of the simulation are presented in the appendix. The solid curves in Fig. 1 show the numerical results of  $\Delta_{\zeta}^2$ , the spectrum of the induced curvature perturbation for  $\beta/H_{\text{inf}} = 4, 5, 10$  and  $20$ , respectively.  $\Delta_{\zeta}^2$  is defined as

$$\Delta_{\zeta}^2(q) = \frac{q^3}{2\pi^2} P_{\zeta}(q) = \frac{q^3}{2\pi^2} \langle \zeta_{\mathbf{q}} \zeta_{\mathbf{q}'}^* \rangle', \quad (18)$$

where  $\langle \dots \rangle'$  denotes the correlation function without the delta function. From Fig. 1, we can see that  $\Delta_{\zeta}^2$  grows as  $q^3$  in the IR region (left of the peak) and drops as  $q^{-6}$  in the UV region (on the far right). By comparing the peak values for the curves of different  $\beta/H_{\text{inf}}$  in Fig. 1, we can also conclude that  $\Delta_{\zeta}^2 \propto (H_{\text{inf}}/\beta)^3$ .

To further illustrate the physics, we will derive an approximate formula for the spectrum of the scalar perturbation. As shown in the appendix, in the parameter space we are interested in, the gravitational-induced contribution to the curvature perturbation is smaller than

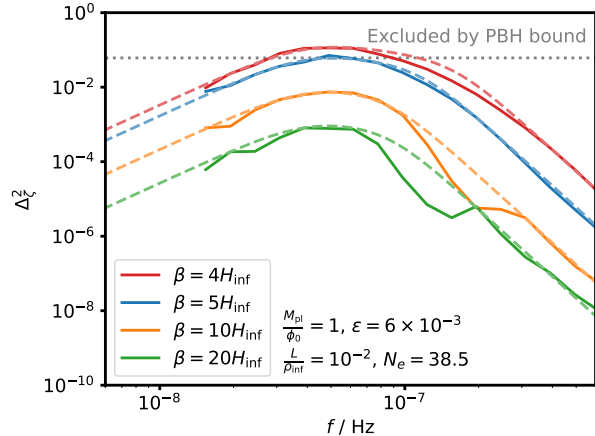


Figure 1. Power spectrum of the induced curvature perturbation,  $\Delta^2(k)$  for different choices of parameters. The solid curves are the results of numerical simulation, and the dashed curves are based on the empirical formula Eq. (23). The wiggles in the curves for  $\beta/H_{\text{inf}} = 10$  and  $20$  are the residual of the oscillation pattern in the integral kernel (17), which also gives the oscillatory pattern in the primary GW spectrum as discussed in [81, 82]. Large curvature perturbation will lead to primordial black hole (PBH) production, and the relevant constraint is indicated by the grey dotted line [86].

the direct contribution. Hence, in the qualitative analysis, we focus on the contribution from the direct source (the first term in  $\mathcal{S}_{\mathbf{q}}$ ). From Eqs. (9) and (16), we have  $\Delta_{\zeta}^2$  must be proportional to  $1/\epsilon$ , where  $\epsilon = \dot{\phi}_0^2 / (2H_{\text{inf}}^2 M_{\text{pl}}^2)$ , is the slow-roll parameter after the phase transition. Here we assume that the fields in the spectator sector are heavy, and after the phase transition, the rolling of the scalar fields is still mostly in the direction of the original inflaton,  $\phi_0$ .  $\zeta_{\mathbf{q}}$  can be estimated as

$$\zeta_{\mathbf{q}} \approx \frac{H_{\text{inf}}}{\dot{\phi}_0} \int \frac{d\tau'}{q^2 \tau'} \left( \cos q\tau' - \frac{\sin q\tau'}{q\tau'} \right) \frac{c_m \phi_0 [\sigma^2(\tau')]_{\mathbf{q}}}{H_{\text{inf}}^2 \tau'^2}. \quad (19)$$

For first-order phase transitions to complete, we require its duration  $\sim \beta^{-1} < H_{\text{inf}}^{-1}$ . However, even after the phase transition, the  $\sigma$  field still oscillates and continues producing  $\zeta$ . Since  $\beta < m_{\sigma}$  so that the oscillations are matter-like, it redshift as  $a^{-3}$ . Thus, the  $\zeta$  production fades within a couple of e-folds after the phase transition. Indeed, Fig. A2 in the appendix shows that most of the induced curvature perturbations are produced between one and two e-folds after the phase transition starts.

Next, we consider the spectrum of scalar perturbation. We begin with the modes with  $q_{\text{phys}} < H_{\text{inf}}$ , or equivalently  $q\tau' < 1$ . In this regime, we can Taylor expand the cosine and sine in the integrand of Eq. 19 and get

$$\zeta_{\mathbf{q}} \approx \frac{1}{3\dot{\phi}_0} \int dt' c_m \phi_0 [\sigma^2(\tau')]_{\mathbf{q}}, \quad (20)$$

where  $dt' = a(\tau')d\tau'$ . Since the typical scale of the bubble size is  $\beta^{-1}$  and  $H_{\text{inf}} < \beta$ , we expect the correlation  $\langle [\sigma^2]_{\mathbf{q}} [\sigma^2]_{\mathbf{q}'} \rangle'$  is insensitive to  $\mathbf{q}$ . Since the term  $c_m \phi_0^2 \sigma^2$  triggers the phase transition in the  $\sigma$  sector, we also expect  $c_m \phi_0^2 \sigma^2 \sim L$ . Hence, we have,

$$\int dt' \int dt'' c_m^2 \phi_0^2 \langle [\sigma^2(\tau')]_{\mathbf{q}} [\sigma^2(\tau'')]_{\mathbf{q}'} \rangle' \sim \frac{L^2}{H_{\text{inf}}^2 a_*^6} \left( \frac{2\pi}{\beta} \right)^3 \quad (21)$$

where  $a_*$  is the scale factor at the time of the phase transition. The factor  $H_{\text{inf}}^{-2}$  is from the integral of the physical time duration, and the factor  $(2\pi/\beta)^3$  is from dimensional analysis. The factor  $a_*^6$  appears in the denominator because the Fourier transformation is in comoving space. Combining (20) and (21), we have, in the region  $q_{\text{phys}} < H_{\text{inf}}$ ,

$$\Delta_\zeta^2(q) = \frac{\mathcal{A}}{\epsilon} \left( \frac{M_{\text{pl}}}{\phi_0} \right)^2 \left( \frac{H_{\text{inf}}}{\beta} \right)^3 \left( \frac{L}{\rho_{\text{inf}}} \right)^2 \left( \frac{q_{\text{phys}}}{H_{\text{inf}}} \right)^3, \quad (22)$$

where  $\mathcal{A}$  collects all the numerical factors. Eq. (22) explains the IR behavior, the  $(H_{\text{inf}}/\beta)^3$  dependence, and the  $(L/\rho_{\text{inf}})^2$  dependence of  $\Delta_\zeta^2$  shown in Fig. 1.

The  $q^3$  growth of  $\Delta_\zeta^2$  stops when  $q_{\text{phys}}$  reaches  $H$ . In the region that  $q_{\text{phys}} \gtrsim H_{\text{inf}}$ , the sine and cosine in (19) are order one, whereas  $\langle [\sigma^2]_{\mathbf{q}} [\sigma^2]_{\mathbf{q}'}^* \rangle'$  is still insensitive to the change of  $q$ . Therefore, by counting the power of  $q$  in this region, we get  $\Delta_\zeta^2$  drops as  $q^{-1}$ .

As shown in the appendix, the production of the curvature perturbation lasts for a couple of e-folds, the typical physical momentum of the bubbles are redshifted, and thus we expect the correlation  $\langle [\sigma^2]_{\mathbf{q}} [\sigma^2]_{\mathbf{q}'}^* \rangle'$  to drop significantly with  $q$  for  $q_{\text{phys}}$  larger than some value between  $H$  and  $\beta$ . From numerical simulation, as shown in Fig. 1,  $\Delta_\zeta^2$  drops as  $q^{-6}$  in the UV region.

In summary, we arrive at an empirical formula for the spectrum of the induced curvature perturbation,

$$\Delta_\zeta^{2(\text{emp})}(q) = A_{\text{ref}} \mathcal{F} \left( \frac{q_{\text{phys}}}{H_{\text{inf}}} \right), \quad (23)$$

where

$$A_{\text{ref}} = \frac{24}{\epsilon} \left( \frac{M_{\text{pl}}}{\phi_0} \right)^2 \left( \frac{H_{\text{inf}}}{\beta} \right)^3 \left( \frac{L}{\rho_{\text{inf}}} \right)^2, \quad (24)$$

$$\mathcal{F}(x) = \frac{x^3}{1 + (\alpha_1 x)^4 + (\alpha_2 x)^9}. \quad (25)$$

From the numerical results, we can get  $\alpha_1 = 0.31$ ,  $\alpha_2$  mildly depends on  $\beta/H_{\text{inf}}$  and equals 0.143, 0.17, 0.2, and 0.2 for  $\beta/H_{\text{inf}} = 4, 5, 10$  and 20.

In a general inflation model,  $\phi_0$  and  $\epsilon$  can be independent parameters. For single field inflation, if we consider the case that  $\partial V_1/\partial\phi$  dominates the evolution of  $\phi_0$  after the phase transition, we have

$$\epsilon = \frac{\dot{\phi}_0^2}{2M_{\text{pl}}^2 H_{\text{inf}}^2} \sim \frac{(V_1')^2}{6\rho_{\text{inf}} H_{\text{inf}}^2}, \quad (26)$$

and, assuming  $V_1$  is a polynomial,

$$\frac{M_{\text{pl}}^2}{\phi_0^2} \sim \left( \frac{M_{\text{pl}}}{V_1/V_1'} \right)^2 \sim \left( \frac{M_{\text{pl}}}{L/V_1'} \right)^2. \quad (27)$$

Thus, without fine-tuning, the peak value of  $\Delta_\zeta^2$  is

$$\Delta_\zeta^2(q) \approx 3.6 \times \left( \frac{H_{\text{inf}}}{\beta} \right)^3 \mathcal{F} \left( \frac{q_{\text{phys}}}{H_{\text{inf}}} \right), \quad (28)$$

Thus, for  $H_{\text{inf}}/\beta \sim 0.1$ , it is natural to expect the peak value of  $\Delta_\zeta^2$  to be around 0.01.

## PRODUCTION OF SECONDARY GW

To produce the GW to account for the PTA results, the curvature perturbations need to reenter the horizon well before the matter-radiation equity. Thus, we have, after inflation,

$$\tilde{\Phi}_{\mathbf{q}}(\tau) = -\frac{2}{3} T(q\tau) \zeta_{\mathbf{q}}, \quad (29)$$

where  $T(q\tau)$  is the RD transfer function. We then use Eqs. (5) and (6) to calculate the secondary GW. Following the standard procedure [84], we can get the spectrum function for the secondary GWs,

$$\Omega_{\text{GW}}^{(2)}(f) = \Omega_R A_{\text{ref}}^2 \mathcal{F}_2 \left( \frac{q_{\text{phys}}}{H_{\text{inf}}} \right), \quad (30)$$

where  $\Omega_R$  is the radiation energy density of the universe. The form factor  $\mathcal{F}_2$  collects the transfer functions and Green's functions. As shown in the appendix, the peak value of  $\mathcal{F}_2$  is about 200, in the IR region, we have

$$\mathcal{F}_2^{\text{IR}}(x) \approx x^3 \left( \frac{6}{5} \log^2 x + \frac{16}{25} \log x + \frac{28}{125} \right). \quad (31)$$

It is the logarithmic structure in  $\mathcal{F}_2$  that slows down the rising of the spectrum and thus gives a fit to IR the NANOGrav observation data as shown in Fig. 2.

The relation between comoving momentum  $q$  and today's frequency  $f$  is

$$f = \frac{q}{2\pi a_0} = f_{\text{ref}} \times \frac{q_{\text{phys}}}{H_{\text{inf}}}, \quad (32)$$

where

$$f_{\text{ref}} = 10^{-9} \text{ Hz} \times e^{40-N_e} \left( \frac{H_{\text{inf}}}{10^{14} \text{ GeV}} \right)^{1/2}, \quad (33)$$

where  $N_e$  is the number of e-folds of phase transition happened before the end of inflation. Here we assume the reheating process finished within one e-fold. Thus, if the phase transition is the reason for the PTA signals, it happened at about 40 e-folds before the end of inflation.

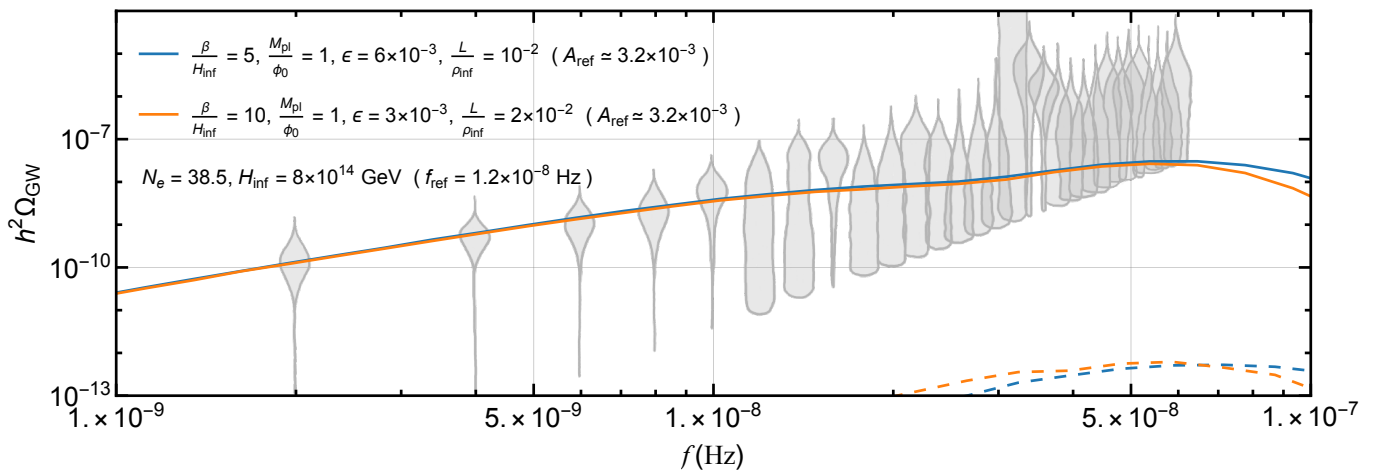


Figure 2. Differential spectra of the secondary GW induced by first-order phase transition during inflation for different parameters as shown in the plot. Two choices of the model parameters are shown as examples. They give the right amplitude to account for the data set collected by the NANOGrav collaboration. They can also fit the spectral shape of the observed data, in particular in the region  $f < 3 \times 10^{-8}$  Hz. As a comparison, the corresponding primary GWs are also shown by the dashed curves. In the interesting parameter region, the magnitude of the primary GWs is smaller than the secondary GWs by a few orders of magnitude.

## SUMMARY AND OUTLOOK

The main result of this work is shown in Fig. 2. As a benchmark, we compare them with data from the NANOGrav collaboration. The observations from the other PTA collaborations are in broad agreement. The secondary GW signal considered in this work can have the same magnitude to account for the observation. They can also fit the spectral shape of the observed data, in particular in the region  $f < 3 \times 10^{-8}$  Hz. Hence, we conclude that the mechanism of GW production studied in this paper provides a promising explanation for the observations made at the PTA collaborations.

The observed signal in the higher frequency range  $f > 3 \times 10^{-8}$  Hz seems to indicate an even higher amplitude. Additional data and the combination of the data from all PTA collaborations can shed more light on this region. In our scenario, we could, in principle, consider slightly later phase transitions (smaller  $N_e$ ) to have the signal peak towards higher frequencies. We can also adjust other parameters, such as  $L$ ,  $\epsilon$ , and  $\beta$ , to a higher amplitude. However, as already evident in Fig. 1, higher amplitudes of curvature perturbation will inevitably lead to copious production of primordial black holes and be in tension with observations. This is a generic limit for any mechanism of secondary GW production.

We expect significant PBH production in the region with large curvature perturbations considered in this work, even if they have not been excluded yet. This could offer a correlated signal to verify the secondary GW production mechanism. We leave a detailed study of this question for future work.

**Acknowledgment**– The work of HA is supported in part by the National Key R&D Program of China under Grants No. 2021YFC2203100 and No. 2017YFA0402204, the NSFC under Grant No. 11975134, and the Tsinghua University Dushi Program No. 53120200422. The work of LTW is supported by the DOE grant DE-SC0013642.

## Appendix

In this appendix, we present the details of the phase transition used in the numerical simulation, the lattice simulation method, and the analysis of the form factor  $\mathcal{F}_2$ .

### DETAILS OF THE NUMERICAL SIMULATION

Here we present the detailed simulation of the evolution of the spectator field  $\sigma$  and the inflaton field  $\phi$  during the first-order phase transition.

#### The phase transition model

In our simulation, the potential in the spectator sector is

$$V_1(\phi, \sigma) = -\frac{1}{2}(m^2 - c_m \phi^2)\sigma^2 + \frac{1}{3}c_3 \sigma^3 + \frac{1}{4}\lambda \sigma^4. \quad (\text{A1})$$

$V_1$  has two non-degenerate local minima,  $\sigma_{\text{fl}}$  and  $\sigma_{\text{tr}}$ . In the earlier time of inflation, when  $c_m \phi_0^2 > m^2$ ,  $\sigma = 0$

is the preferred vacuum. During the slow-roll inflation,  $\phi_0$  becomes smaller, the phase transition happens when  $c_m \phi_0^2 < m^2$ .

The cubic term in the potential  $V_1$  provides a barrier between the true and false vacua, and thus the phase transition is first-order. The bubble nucleation process is described by the bounce solution,  $\sigma_b$  [87, 88], which satisfies the Euclidean field equation,

$$\frac{d^2 \sigma_b}{dr^2} + \frac{3}{r} \frac{d\sigma_b}{dr} = \frac{dV_1}{d\sigma_b}, \quad (\text{A2})$$

where in Euclidean space  $r = (t^2 + \mathbf{x}^2)^{1/2}$  and  $dr^2 = dt^2 + d\mathbf{x}^2$ . In Eq. (A2), the Hubble expansion is ignored, since typical energy scale of the spectator sector in this study is much larger than  $H_{\text{inf}}$ . The boundary conditions for the Euclidean equation of motion (A2) are

$$\sigma_b(\infty) = \sigma_{\text{fl}}, \quad \left. \frac{d\sigma_b}{dr} \right|_{r=0} = 0, \quad (\text{A3})$$

and then the bubble nucleation rate per unit physical volume can be written as

$$\frac{\Gamma}{V_{\text{phys}}} \sim m^4 e^{-S_b}, \quad (\text{A4})$$

where the Euclidean bounce action  $S_b$  is

$$S_b = 2\pi^2 \int_0^\infty dr r^3 \left[ \frac{1}{2} \left( \frac{d\sigma_b}{dr} \right)^2 + V_1(\phi_0, \sigma_b) - V_1(\phi_0, \sigma_{\text{fl}}) \right] \quad (\text{A5})$$

The initial configuration of the bubbles in Minkowski space are then given by the analytical continuation of bounce solution to the Minkowski space,  $\sigma_b(r) \rightarrow \sigma_b(\sqrt{a^2(\mathbf{x}^2 - \tau^2)})$ . Then we use the classical field equation,

$$\sigma'' + 2\mathcal{H}\sigma' - \nabla^2 \sigma + a^2 \frac{dV_1}{d\sigma} = 0, \quad (\text{A6})$$

to calculate the evolution of the  $\sigma$  field.

### Lattice simulation

We discretize the space using a cubic lattice with  $N$  grids per spatial dimension. The  $N^3$  points are labeled as

$$\mathbf{n} = (n_1, n_2, n_3), \quad \text{with } n_i = 0, 1, \dots, N-1, \quad i = 1, 2, 3. \quad (\text{A7})$$

In the simulation, a field defined on the continuum space with comoving coordinate  $\mathbf{x}$ ,  $f(\mathbf{x})$ , is converted to a field defined  $f(\mathbf{n})$  defined on the lattice, with the condition,

$f(\mathbf{x})$  at  $\mathbf{x} = \mathbf{n}\delta x$ . Note that in our simulation, the lattice is defined in coordinate system. For convenience, we set  $m = 1$  hereafter. In this unit, the Hubble constant  $H_{\text{inf}}$  has the value 0.01. The physical size of the lattice spacing  $\delta x$  is set to be 0.6 at the beginning of the simulation. We proved that 0.6 is small enough to give accurate secondary GW signals by comparing the results between  $\delta x = 0.6$  to  $\delta x = 0.3$  with the same total volume.

In our simulation,  $N = 1183$ , thus the size of the whole space is  $7H_{\text{inf}}^{-1}$ . In the simulation, we use periodic boundary conditions in the three spatial directions, so that  $f(\mathbf{n} + \mathbf{e}_i N) = f(\mathbf{n})$ , where  $\mathbf{e}_i$  denotes one of the unit vectors in the three spatial dimensions.

Note that the finite volume of the cubic lattice implies an IR cut-off of momenta

$$\delta k = \frac{2\pi}{N\delta x}, \quad (\text{A8})$$

and therefore the momenta must be discretized. The finite spatial volume and the discretization require discrete Fourier transformation,

$$f(\tilde{\mathbf{n}}) = \sum_{\mathbf{n}} (\delta x)^3 f(\mathbf{n}) e^{-i\frac{2\pi}{N}\mathbf{n}\cdot\tilde{\mathbf{n}}},$$

$$f(\mathbf{n}) = \sum_{\tilde{\mathbf{n}}} \left( \frac{\delta k}{2\pi} \right)^3 f(\tilde{\mathbf{n}}) e^{i\frac{2\pi}{N}\tilde{\mathbf{n}}\cdot\mathbf{n}}, \quad (\text{A9})$$

where the momenta are also periodic, so practically we choose

$$\tilde{\mathbf{n}} = (\tilde{n}_1, \tilde{n}_2, \tilde{n}_3), \quad \text{with } \tilde{n}_i = -\frac{N-1}{2}, \dots, \frac{N-1}{2}. \quad (\text{A10})$$

and the corresponding comoving momenta are

$$\mathbf{k} = (k_1, k_2, k_3), \quad \text{with } k_i = -\frac{N-1}{N} \frac{\pi}{\delta x}, \dots, \frac{N-1}{N} \frac{\pi}{\delta x}. \quad (\text{A11})$$

For time evolution, we set the scale factor  $a(\tau_*) = 1$  at the starting time of the simulation, so the conformal time  $\tau_* = -H_{\text{inf}}^{-1}$ . The temporal step is chosen different in each e-fold. In practice, the phase transition completes in at most 5 e-folds, and we split the first one into 1000 steps, the second one into 500 steps, the third one into 250 steps, the fourth one into 125 steps, and the last one into 60 steps.

To facilitate the numerical simulation, we redefine the fields and parameters in the theory as

$$\sigma \rightarrow \frac{\sigma}{\sqrt{\lambda}}, \quad \phi \rightarrow \frac{\phi}{\sqrt{c_m}}, \quad c_3 \rightarrow \sqrt{\lambda} c_3. \quad (\text{A12})$$

Then Eq. (A1) becomes

$$V_1(\phi, \sigma) = \frac{1}{\lambda} \left[ -\frac{1}{2} (1 - \phi^2) \sigma^2 + \frac{1}{3} c_3 \sigma^3 + \frac{1}{4} \sigma^4 \right], \quad (\text{A13})$$

and the field equation Eq.(A6) can be rewritten as

$$\sigma'' + 2\mathcal{H}\sigma' - \nabla^2\sigma + a^2[-(1-\phi^2)\sigma + c_3\sigma^2 + \sigma^3] = 0. \quad (\text{A14})$$

To ensure the phase transition can take place and complete in acceptable time, the action  $S_b$  should not be too large, which we keep under 20. Under this requirement and the slow-roll condition, we set the quartic interaction coefficient  $\lambda = 2$ , the cubic coefficient  $c_3 = 1$ , the initial value of the inflaton  $\phi_0(\tau_0) = 1.03$ , and then tune the initial velocity of the inflaton  $\dot{\phi}_0(\tau_0)$  to adjust the value of  $\beta$ .

The starting time of simulation,  $t_*$ , is defined as the moment when there is roughly one bubble nucleated per Hubble volume, which means

$$\frac{\Gamma(t_*)}{V_{\text{phys}}} \simeq H_{\text{inf}}^4. \quad (\text{A15})$$

During the phase transition, the bubble nucleation rate can be parameterized as

$$\Gamma(t) \simeq \Gamma(t_*)e^{\beta(t-t_*)}, \quad (\text{A16})$$

where

$$\beta \equiv - \left. \frac{dS_b}{dt} \right|_{t=t_*}. \quad (\text{A17})$$

Here  $t$  denotes the physical time. The initial condition of  $\sigma$  is chosen as

$$\sigma = \sigma_{\text{fl}}, \quad \sigma' = 0. \quad (\text{A18})$$

we simulate the process of phase transition using the classical equation of  $\sigma$ . This field is evolved by the same numerical integrator used in [89, 90], (the details can also be found in the appendix of [91]). In the case of this work, the Hamiltonian that governs the evolution of the system is

$$\mathcal{H} = \int d^3\mathbf{x} \frac{1}{2} \left[ \frac{1}{a^2} \pi^2 + a^2 (\nabla\sigma)^2 + a^4 V_1(\phi, \sigma) \right], \quad (\text{A19})$$

where  $\pi \equiv a^2\sigma'$ .

During the simulation, the bubbles are generated in the region still occupied by the false vacuum at the beginning of each temporal step. The number density of the bubbles generated at each temporal step is calculated by the nucleation rate per unit lattice volume and the positions of bubble centers are chosen randomly.

At each temporal step, the probability for a bubble to be produced on each site follows the binomial distribution with the probability,

$$p = \frac{\Gamma(\tau)}{V_{\text{phys}}} \delta x^3 \delta\tau a^4(\tau). \quad (\text{A20})$$

Thus, in practice, at each temporal step, we generate random numbers that obey the binomial distribution with

probability  $p$  at the sites that are still occupied by the false vacuum to decide whether the true vacuum bubbles can be generated at that site. The profile of the bubbles is determined by the bounce solution  $\sigma_b$ .

After nucleation, the bubbles will expand rapidly, then collide with each other and finally occupy the whole space. Fig. A1 shows the evolution of ratio  $\sigma_0/\sigma_{\text{tr}}$ , where  $\sigma_0$  is the mean value of the  $\sigma$  field. This value reflects the occupation fraction of the true vacuum since the false vacuum of our system is set to be  $\sigma_{\text{fl}} = 0$ . Fig. A1 shows that the bubble collision process is finished within a couple of  $\beta^{-1}$ .

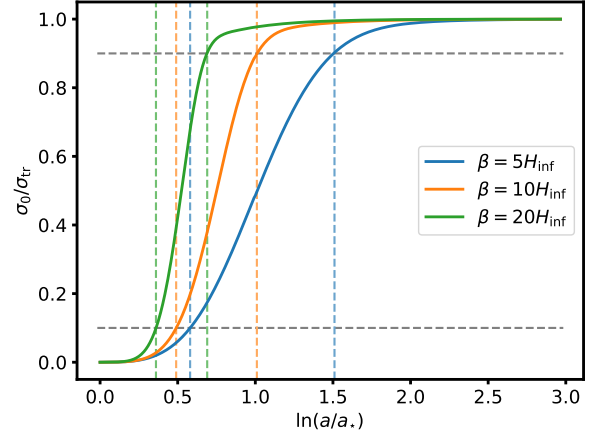


Figure A1. The mean value of  $\sigma$ . The dashed horizontal lines label the situation 10% (down) or 90% (up) of the space is occupied by the true vacuum while the dashed vertical lines label the moment at which the system reach such situation.

With the  $\sigma$  field configuration at each temporal step, we calculate  $\delta\phi$ ,  $\Psi$  and  $\Phi$  by solving the differential equations (7) and (10) together with the conditions (8), (11) and (12).

Notice that  $\delta\phi$  contributes to the source term of  $\Psi$  in Eq. (10), so we can't finish the integral Eq.(13) directly using the Green's function method described in the main text for the qualitative analysis. In the numerical simulation, the differential equations are in an iterative way. In detail, at each temporal step, we use  $\sigma$ ,  $\delta\phi$ ,  $\Psi$  and  $\Phi$  from the last step to calculate the source function (8), (10) and (12). And use the source to calculate the evolution of  $\delta\phi$ ,  $\Psi$ , and  $\Phi$  in the current step. We do this calculation iteratively to obtain the evolution of  $\delta\phi$ ,  $\Psi$ , and  $\Phi$ .

After the phase transition, we calculate the curvature perturbation  $\zeta$  using Eq. (15), and the power spectrum  $\Delta_\zeta^2$ . Fig. A2 shows the accumulated contributions to  $\Delta_\zeta^2$ , where for each curve the  $\tau'$  integral is from  $\tau_*$  to the value indicated in the figure. The parameters are chosen to be  $\beta/H = 5$ ,  $L/\rho_{\text{inf}} = 10^{-2}$ ,  $M_{\text{pl}}/\phi_0 = 1$ ,  $\epsilon = 6 \times 10^{-3}$ . We can see that the induced curvature perturbation are

mostly produced between one and two e-folds after the phase transition. Therefore, the physical duration of the production of the curvature perturbation is about  $H^{-1}$ .

Fig.(A3) shows the induced curvature spectrum  $\Delta_{\zeta}^2$  for different choices of  $\beta/H$ , together with pure gravitational contributions shown in the dashed curves. we can see that the gravitational contributions are negligible compared to the direct contributions.

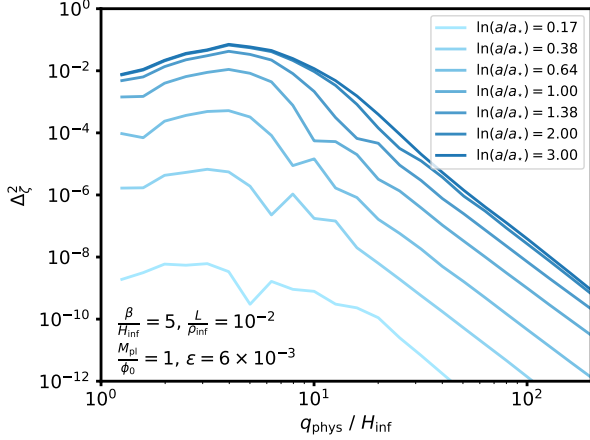


Figure A2. Accumulated contributions to the induced curvature perturbation, with the  $\tau'$  integral stops at the values shown in the legend for each curve.

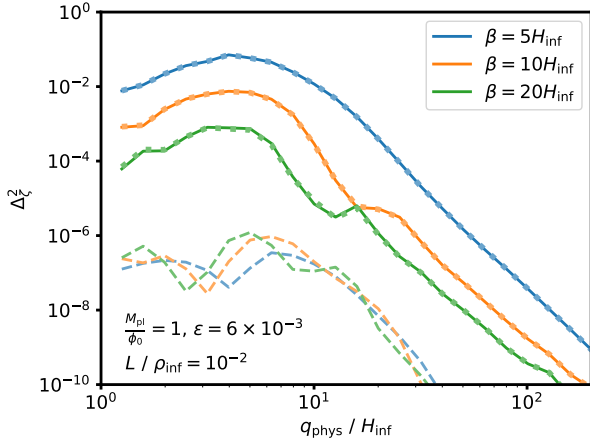


Figure A3. The power spectra of curvature perturbation of  $\beta = 5H_{\text{inf}}$  (blue),  $\beta = 10H_{\text{inf}}$  (orange) and  $\beta = 20H_{\text{inf}}$  (green). The dotted line shows the contribution from direct coupling and the dashed line shows the pure gravitational contribution, while the full results are shown by the solid line. We can see the solid line and the dotted line are almost overlapped.

## DETAILS OF THE SHAPE FUNCTION $\mathcal{F}_2$

For the curvature perturbation to reenter the horizon well before the matter-radiation equality, the GWs observed today are mainly produced during radiation dominated era. Thus the energy fraction of GWs can be written as [84]

$$\Omega_{\text{GW}}(k) = \Omega_{\text{rad}} \frac{k^3}{6} \int_0^\infty dk_1 \int_{-1}^1 d\mu \frac{k_1^3}{k_2^3} (1 - \mu^2)^2 \cdot \bar{I}^2(k, k_1, k_2) \mathcal{P}_\zeta(k_1) \mathcal{P}_\zeta(k_2), \quad (\text{A21})$$

where  $\bar{I}^2(k, k_1, k_2)$  is the integration kernel

$$\begin{aligned} \bar{I}^2(k, k_1, k_2) &= \frac{1}{2} \left( \frac{3(k_1^2 + k_2^2 - 3k^2)}{4k_1^3 k_2^3} \right)^2 \\ &\times \left\{ \pi^2 (k_1^2 + k_2^2 - 3k^2)^2 \theta(k_1 + k_2 - \sqrt{3}k) \right. \\ &\left. + \left[ -4k_1 k_2 + (k_1^2 + k_2^2 - 3k^2) \log \left| \frac{3k^2 - (k_1 + k_2)^2}{3k^2 - (k_1 - k_2)^2} \right| \right]^2 \right\}. \quad (\text{A22}) \end{aligned}$$

with  $\mathbf{k} = \mathbf{k}_1 + \mathbf{k}_2$  and  $\mu = \frac{\mathbf{k} \cdot \mathbf{k}_1}{k k_1}$ . It's convenient to introduce a new variable  $v = k_1/k$ , then we have

$$\Omega_{\text{GW}}(k) = \Omega_{\text{rad}} \int_0^\infty dv \int_{-1}^1 d\mu (1 - \mu^2)^2 \mathcal{K}(v, \mu) \cdot \mathcal{P}_\zeta(vk) \mathcal{P}_\zeta(\sqrt{v^2 + 1 - 2v\mu}k), \quad (\text{A23})$$

where

$$\mathcal{K}(v, \mu) \equiv \frac{v^3 \bar{I}^2(1, v, \sqrt{v^2 + 1 - 2v\mu})}{6 (v^2 + 1 - 2v\mu)^{3/2}}. \quad (\text{A24})$$

Notice the asymptotic behaviors of  $\mathcal{K}(v, \mu)$  is well approximated by

$$\mathcal{K}(v, \mu) \simeq \begin{cases} v^3/3 & v \ll 1 \\ 3v^{-4} \log^2 v & v \gg 1 \end{cases}, \quad (\text{A25})$$

which is independent of  $\mu$ . The shape function  $\mathcal{F}_2$  defined in the main text can be calculated by

$$\mathcal{F}_2(x) = \int_0^\infty dv \int_{-1}^1 d\mu (1 - \mu^2)^2 \mathcal{K}(v, \mu) \cdot \mathcal{F}(vx) \mathcal{F}(\sqrt{v^2 + 1 - 2v\mu}x), \quad (\text{A26})$$

where

$$\mathcal{F}(x) = \frac{x^3}{1 + (\alpha_1 x)^4 + (\alpha_2 x)^9} \quad (\text{A27})$$

is the form factor for  $\Delta_{\zeta}^2$ . We assume  $\mathcal{F}(x)$  has a maximum value  $\mathcal{F}_{\text{max}}$  with coordinate  $x_{\text{max}}$ , and it can be approximated as

$$\mathcal{F}(x) \simeq \begin{cases} \mathcal{F}_{\text{max}}(x/x_{\text{max}})^3 & x < x_{\text{max}} \\ \mathcal{F}_{\text{max}}(x/x_{\text{max}})^{-6} & x \gg x_{\text{max}} \end{cases} \quad (\text{A28})$$



Now we consider the asymptotic behaviors of  $\mathcal{F}_2$ . The  $v$  integral is most donated around  $vx \simeq x_{\max}$  i.e. when  $\mathcal{F}(x)$  achieved its maximum value, since the descent of  $\mathcal{F}(x)$  is deeper then  $\mathcal{K}(v, \mu)$ . For small  $x$ ,  $v \simeq x_{\max}/x \gg 1$ ,  $\sqrt{v^2 + 1} - 2v\mu \simeq v$ , then the integral becomes

$$\begin{aligned} \mathcal{F}_2(x) &\simeq \mathcal{F}_{\max}^2 \left\{ \int_0^{x_{\max}/x} dv 3v^{-4} \log^2 v \cdot (vx/x_{\max})^6 \right. \\ &\quad \left. + \int_{x_{\max}/x}^{\infty} dv 3v^{-4} \log^2 v \cdot (vx/x_{\max})^{-12} \right\} \\ &\simeq \mathcal{F}_{\max}^2 (x/x_{\max})^3 \log^2(x/x_{\max}), \end{aligned} \quad (\text{A29})$$

where the  $\mu$  integral is factorized and the result is a  $\mathcal{O}(1)$  number. And for large  $x$ ,  $v \simeq x_{\max}/x \ll 1$ ,  $\sqrt{v^2 + 1} - 2v\mu \simeq 1$ . Similarly, we finish the integration and get

$$\begin{aligned} \mathcal{F}_2(x) &\simeq \mathcal{F}_{\max}^2 \left\{ \int_0^{x_{\max}/x} dv v^3/3 \cdot (vx/x_{\max})^3 (x/x_{\max})^{-6} \right. \\ &\quad \left. + \int_{x_{\max}/x}^{\infty} dv v^3/3 \cdot (vx/x_{\max})^{-6} (x/x_{\max})^{-6} \right\} \\ &\simeq \mathcal{F}_{\max}^2 (x/x_{\max})^{-10}. \end{aligned} \quad (\text{A30})$$

In the parameter space we interested, we have  $\mathcal{F}_{\max} \simeq \mathcal{O}(10)$ , so the peak value of  $\mathcal{F}_2(x)$  is roughly  $\mathcal{O}(100)$ . The shape of  $\mathcal{F}_2(x)$  for  $\beta/H_{\text{inf}} = 4, 5, 10, 20$  is shown in Fig.(A4). We can see a shoulder in the left of the peak which is from the contribution of logarithmic function. This shoulder will slow down the slope of this region significantly.

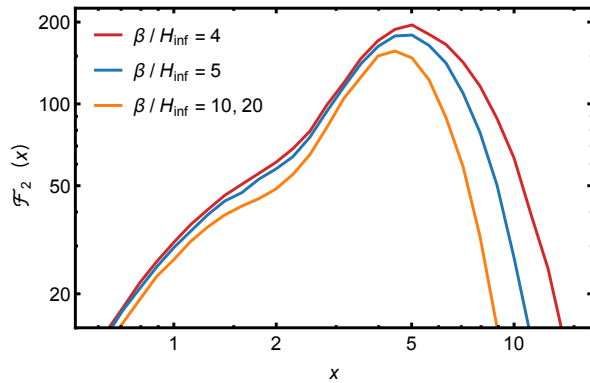


Figure A4. The shape function  $\mathcal{F}_2(x)$  of  $\beta = 4H_{\text{inf}}$  (red),  $\beta = 5H_{\text{inf}}$  (blue) and  $\beta = 10, 20$  (orange).

<sup>†</sup> sby20@mails.tsinghua.edu.cn

<sup>‡</sup> hanwentai@uchicago.edu

<sup>§</sup> liantaow@uchicago.edu

<sup>¶</sup> yangc18@mails.tsinghua.edu.cn

- [1] **NANOGrav** Collaboration, G. Agazie *et al.*, “The NANOGrav 15 yr Data Set: Observations and Timing of 68 Millisecond Pulsars,” *Astrophys. J. Lett.* **951** no. 1, (2023) L9, [arXiv:2306.16217 \[astro-ph.HE\]](#).
- [2] J. Antoniadis *et al.*, “The second data release from the European Pulsar Timing Array I. The dataset and timing analysis,” [arXiv:2306.16224 \[astro-ph.HE\]](#).
- [3] A. Zic *et al.*, “The Parkes Pulsar Timing Array Third Data Release,” [arXiv:2306.16230 \[astro-ph.HE\]](#).
- [4] H. Xu *et al.*, “Searching for the Nano-Hertz Stochastic Gravitational Wave Background with the Chinese Pulsar Timing Array Data Release I,” *Res. Astron. Astrophys.* **23** no. 7, (2023) 075024, [arXiv:2306.16216 \[astro-ph.HE\]](#).
- [5] **NANOGrav** Collaboration, G. Agazie *et al.*, “The NANOGrav 15 yr Data Set: Evidence for a Gravitational-wave Background,” *Astrophys. J. Lett.* **951** no. 1, (2023) L8, [arXiv:2306.16213 \[astro-ph.HE\]](#).
- [6] J. Antoniadis *et al.*, “The second data release from the European Pulsar Timing Array III. Search for gravitational wave signals,” [arXiv:2306.16214 \[astro-ph.HE\]](#).
- [7] D. J. Reardon *et al.*, “Search for an Isotropic Gravitational-wave Background with the Parkes Pulsar Timing Array,” *Astrophys. J. Lett.* **951** no. 1, (2023) L6, [arXiv:2306.16215 \[astro-ph.HE\]](#).
- [8] R. w. Hellings and G. s. Downs, “UPPER LIMITS ON THE ISOTROPIC GRAVITATIONAL RADIATION BACKGROUND FROM PULSAR TIMING ANALYSIS,” *Astrophys. J. Lett.* **265** (1983) L39–L42.
- [9] G. Franciolini, D. Racco, and F. Rompineve, “Footprints of the QCD Crossover on Cosmological Gravitational Waves at Pulsar Timing Arrays,” [arXiv:2306.17136 \[astro-ph.CO\]](#).
- [10] L. Zu, C. Zhang, Y.-Y. Li, Y.-C. Gu, Y.-L. S. Tsai, and Y.-Z. Fan, “Mirror QCD phase transition as the origin of the nanohertz Stochastic Gravitational-Wave Background detected by the Pulsar Timing Arrays,” [arXiv:2306.16769 \[astro-ph.HE\]](#).
- [11] C. Han, K.-P. Xie, J. M. Yang, and M. Zhang, “Self-interacting dark matter implied by nano-Hertz gravitational waves,” [arXiv:2306.16966 \[hep-ph\]](#).
- [12] K. Fujikura, S. Girmohanta, Y. Nakai, and M. Suzuki, “NANOGrav Signal from a Dark Conformal Phase Transition,” [arXiv:2306.17086 \[hep-ph\]](#).
- [13] P. Athron, A. Fowlie, C.-T. Lu, L. Morris, L. Wu, Y. Wu, and Z. Xu, “Can Supercooled Phase Transitions explain the Gravitational Wave Background observed by Pulsar Timing Arrays?,” [arXiv:2306.17239 \[hep-ph\]](#).
- [14] A. Addazi, Y.-F. Cai, A. Marciano, and L. Visinelli, “Have pulsar timing array methods detected a cosmological phase transition?,” [arXiv:2306.17205 \[astro-ph.CO\]](#).
- [15] S. Jiang, A. Yang, J. Ma, and F. P. Huang, “Implication of nano-Hertz stochastic gravitational wave on dynamical dark matter through a first-order phase transition,” [arXiv:2306.17827 \[hep-ph\]](#).
- [16] K. Murai and W. Yin, “A Novel Probe of Supersymmetry in Light of Nanohertz Gravitational

\* anhp@mail.tsinghua.edu.cn

- Waves,” [arXiv:2307.00628 \[hep-ph\]](#).
- [17] S.-P. Li and K.-P. Xie, “A collider test of nano-Hertz gravitational waves from pulsar timing arrays,” [arXiv:2307.01086 \[hep-ph\]](#).
- [18] Y. Xiao, J. M. Yang, and Y. Zhang, “Implications of Nano-Hertz Gravitational Waves on Electroweak Phase Transition in the Singlet Dark Matter Model,” [arXiv:2307.01072 \[hep-ph\]](#).
- [19] T. Ghosh, A. Ghoshal, H.-K. Guo, F. Hajkarim, S. F. King, K. Sinha, X. Wang, and G. White, “Did we hear the sound of the Universe boiling? Analysis using the full fluid velocity profiles and NANOGrav 15-year data,” [arXiv:2307.02259 \[astro-ph.HE\]](#).
- [20] K. T. Abe and Y. Tada, “Translating nano-Hertz gravitational wave background into primordial perturbations taking account of the cosmological QCD phase transition,” [arXiv:2307.01653 \[astro-ph.CO\]](#).
- [21] X. K. Du, M. X. Huang, F. Wang, and Y. K. Zhang, “Did the nHZ Gravitational Waves Signatures Observed By NANOGrav Indicate Multiple Sector SUSY Breaking?,” [arXiv:2307.02938 \[hep-ph\]](#).
- [22] Y.-M. Wu, Z.-C. Chen, and Q.-G. Huang, “Cosmological Interpretation for the Stochastic Signal in Pulsar Timing Arrays,” [arXiv:2307.03141 \[astro-ph.CO\]](#).
- [23] X.-F. Li, “Probing the high temperature symmetry breaking with gravitational waves from domain walls,” [arXiv:2307.03163 \[hep-ph\]](#).
- [24] J. S. Cruz, F. Niedermann, and M. S. Sloth, “NANOGrav meets Hot New Early Dark Energy and the origin of neutrino mass,” [arXiv:2307.03091 \[astro-ph.CO\]](#).
- [25] P. Di Bari and M. H. Rahat, “The split majoron model confronts the NANOGrav signal,” [arXiv:2307.03184 \[hep-ph\]](#).
- [26] Y. Gouttenoire, “First-order Phase Transition interpretation of PTA signal produces solar-mass Black Holes,” [arXiv:2307.04239 \[hep-ph\]](#).
- [27] A. Salvio, “Supercooling in Radiative Symmetry Breaking: Theory Extensions, Gravitational Wave Detection and Primordial Black Holes,” [arXiv:2307.04694 \[hep-ph\]](#).
- [28] Z.-Q. Shen, G.-W. Yuan, Y.-Y. Wang, and Y.-Z. Wang, “Dark Matter Spike surrounding Supermassive Black Holes Binary and the nanohertz Stochastic Gravitational Wave Background,” [arXiv:2306.17143 \[astro-ph.HE\]](#).
- [29] S.-Y. Guo, M. Khlopov, X. Liu, L. Wu, Y. Wu, and B. Zhu, “Footprints of Axion-Like Particle in Pulsar Timing Array Data and JWST Observations,” [arXiv:2306.17022 \[hep-ph\]](#).
- [30] G. Franciolini, A. Iovino, Junior., V. Vaskonen, and H. Veermäe, “The recent gravitational wave observation by pulsar timing arrays and primordial black holes: the importance of non-gaussianities,” [arXiv:2306.17149 \[astro-ph.CO\]](#).
- [31] J. Ellis, M. Fairbairn, G. Hütsi, J. Raidal, J. Urrutia, V. Vaskonen, and H. Veermäe, “Gravitational Waves from SMBH Binaries in Light of the NANOGrav 15-Year Data,” [arXiv:2306.17021 \[astro-ph.CO\]](#).
- [32] T. Broadhurst, C. Chen, T. Liu, and K.-F. Zheng, “Binary Supermassive Black Holes Orbiting Dark Matter Solitons: From the Dual AGN in UGC4211 to NanoHertz Gravitational Waves,” [arXiv:2306.17821 \[astro-ph.HE\]](#).
- [33] H.-L. Huang, Y. Cai, J.-Q. Jiang, J. Zhang, and Y.-S. Piao, “Supermassive primordial black holes in multiverse: for nano-Hertz gravitational wave and high-redshift JWST galaxies,” [arXiv:2306.17577 \[gr-qc\]](#).
- [34] Y.-C. Bi, Y.-M. Wu, Z.-C. Chen, and Q.-G. Huang, “Implications for the Supermassive Black Hole Binaries from the NANOGrav 15-year Data Set,” [arXiv:2307.00722 \[astro-ph.CO\]](#).
- [35] C. Zhang, N. Dai, Q. Gao, Y. Gong, T. Jiang, and X. Lu, “Detecting new fundamental fields with Pulsar Timing Arrays,” [arXiv:2307.01093 \[gr-qc\]](#).
- [36] Y. Gouttenoire, S. Trifunopoulos, G. Valogiannis, and M. Vanvlasselaer, “Scrutinizing the Primordial Black Holes Interpretation of PTA Gravitational Waves and JWST Early Galaxies,” [arXiv:2307.01457 \[astro-ph.CO\]](#).
- [37] Z. Wang, L. Lei, H. Jiao, L. Feng, and Y.-Z. Fan, “The nanohertz stochastic gravitational-wave background from cosmic string Loops and the abundant high redshift massive galaxies,” [arXiv:2306.17150 \[astro-ph.HE\]](#).
- [38] J. Ellis, M. Lewicki, C. Lin, and V. Vaskonen, “Cosmic Superstrings Revisited in Light of NANOGrav 15-Year Data,” [arXiv:2306.17147 \[astro-ph.CO\]](#).
- [39] N. Kitajima, J. Lee, K. Murai, F. Takahashi, and W. Yin, “Nanohertz Gravitational Waves from Axion Domain Walls Coupled to QCD,” [arXiv:2306.17146 \[hep-ph\]](#).
- [40] Y. Bai, T.-K. Chen, and M. Korwar, “QCD-Collapsed Domain Walls: QCD Phase Transition and Gravitational Wave Spectroscopy,” [arXiv:2306.17160 \[hep-ph\]](#).
- [41] N. Kitajima and K. Nakayama, “Nanohertz gravitational waves from cosmic strings and dark photon dark matter,” [arXiv:2306.17390 \[hep-ph\]](#).
- [42] G. Lazarides, R. Maji, and Q. Shafi, “Superheavy quasi-stable strings and walls bounded by strings in the light of NANOGrav 15 year data,” [arXiv:2306.17788 \[hep-ph\]](#).
- [43] P. F. Depta, K. Schmidt-Hoberg, and C. Tassilo, “Do pulsar timing arrays observe merging primordial black holes?,” [arXiv:2306.17836 \[astro-ph.CO\]](#).
- [44] L. Bian, S. Ge, J. Shu, B. Wang, X.-Y. Yang, and J. Zong, “Gravitational wave sources for Pulsar Timing Arrays,” [arXiv:2307.02376 \[astro-ph.HE\]](#).
- [45] B. Barman, D. Borah, S. Jyoti Das, and I. Saha, “Scale of Dirac leptogenesis and left-right symmetry in the light of recent PTA results,” [arXiv:2307.00656 \[hep-ph\]](#).
- [46] S. Antusch, K. Hinze, S. Saad, and J. Steiner, “Singling out SO(10) GUT models using recent PTA results,” [arXiv:2307.04595 \[hep-ph\]](#).
- [47] E. Babichev, D. Gorbunov, S. Ramazanov, R. Samanta, and A. Vikman, “NANOGrav spectral index  $\gamma = 3$  from melting domain walls,” [arXiv:2307.04582 \[hep-ph\]](#).
- [48] W. Buchmuller, V. Domcke, and K. Schmitz, “Metastable cosmic strings,” [arXiv:2307.04691 \[hep-ph\]](#).
- [49] M. Yamada and K. Yonekura, “Dark baryon from pure Yang-Mills theory and its GW signature from cosmic strings,” [arXiv:2307.06586 \[hep-ph\]](#).

- [50] S. Ge, “Stochastic gravitational wave background: birth from axionic string-wall death,” [arXiv:2307.08185 \[gr-qc\]](#).
- [51] Z. Zhang, C. Cai, Y.-H. Su, S. Wang, Z.-H. Yu, and H.-H. Zhang, “Nano-Hertz gravitational waves from collapsing domain walls associated with freeze-in dark matter in light of pulsar timing array observations,” [arXiv:2307.11495 \[hep-ph\]](#).
- [52] S. Vagnozzi, “Inflationary interpretation of the stochastic gravitational wave background signal detected by pulsar timing array experiments,” [arXiv:2306.16912 \[astro-ph.CO\]](#).
- [53] V. K. Oikonomou, “Flat Energy Spectrum of Primordial Gravitational Waves vs Peaks and the NANOGrav 2023 Observation,” [arXiv:2306.17351 \[astro-ph.CO\]](#).
- [54] S. Datta, “Inflationary gravitational waves, pulsar timing data and low-scale leptogenesis,” [arXiv:2307.00646 \[hep-ph\]](#).
- [55] D. Borah, S. Jyoti Das, and R. Samanta, “Inflationary origin of gravitational waves with  $\text{WIMP}$  dark matter in the light of recent PTA results,” [arXiv:2307.00537 \[hep-ph\]](#).
- [56] S. Wang, Z.-C. Zhao, J.-P. Li, and Q.-H. Zhu, “Exploring the Implications of 2023 Pulsar Timing Array Datasets for Scalar-Induced Gravitational Waves and Primordial Black Holes,” [arXiv:2307.00572 \[astro-ph.CO\]](#).
- [57] B.-M. Gu, F.-W. Shu, and K. Yang, “Inflation with shallow dip and primordial black holes,” [arXiv:2307.00510 \[astro-ph.CO\]](#).
- [58] D. Chowdhury, G. Tasinato, and I. Zavala, “Dark energy, D-branes, and Pulsar Timing Arrays,” [arXiv:2307.01188 \[hep-th\]](#).
- [59] X. Niu and M. H. Rahat, “NANOGrav signal from axion inflation,” [arXiv:2307.01192 \[hep-ph\]](#).
- [60] R. Ebadi, S. Kumar, A. McCune, H. Tai, and L.-T. Wang, “Gravitational Waves from Stochastic Scalar Fluctuations,” [arXiv:2307.01248 \[astro-ph.CO\]](#).
- [61] Z. Yi, Q. Gao, Y. Gong, Y. Wang, and F. Zhang, “The waveform of the scalar induced gravitational waves in light of Pulsar Timing Array data,” [arXiv:2307.02467 \[gr-qc\]](#).
- [62] D. G. Figueroa, M. Pieroni, A. Ricciardone, and P. Simakachorn, “Cosmological Background Interpretation of Pulsar Timing Array Data,” [arXiv:2307.02399 \[astro-ph.CO\]](#).
- [63] C. Unal, A. Papageorgiou, and I. Obata, “Axion-Gauge Dynamics During Inflation as the Origin of Pulsar Timing Array Signals and Primordial Black Holes,” [arXiv:2307.02322 \[astro-ph.CO\]](#).
- [64] H. Firouzjahi and A. Talebian, “Induced Gravitational Waves from Ultra Slow-Roll Inflation and Pulsar Timing Arrays Observations,” [arXiv:2307.03164 \[gr-qc\]](#).
- [65] Q.-H. Zhu, Z.-C. Zhao, and S. Wang, “Joint implications of BBN, CMB, and PTA Datasets for Scalar-Induced Gravitational Waves of Second and Third orders,” [arXiv:2307.03095 \[astro-ph.CO\]](#).
- [66] S. Choudhury, “Single field inflation in the light of NANOGrav 15-year Data: Quintessential interpretation of blue tilted tensor spectrum through Non-Bunch Davies initial condition,” [arXiv:2307.03249 \[astro-ph.CO\]](#).
- [67] Z.-Q. You, Z. Yi, and Y. Wu, “Constraints on primordial curvature power spectrum with pulsar timing arrays,” [arXiv:2307.04419 \[gr-qc\]](#).
- [68] S. A. Hosseini Mansoori, F. Felegray, A. Talebian, and M. Sami, “PBHs and GWs from  $T^2$ -inflation and NANOGrav 15-year data,” [arXiv:2307.06757 \[astro-ph.CO\]](#).
- [69] K. Cheung, C. J. Ouseph, and P.-Y. Tseng, “NANOGrav Signal and PBH from the Modified Higgs Inflation,” [arXiv:2307.08046 \[hep-ph\]](#).
- [70] S. Basilakos, D. V. Nanopoulos, T. Papanikolaou, E. N. Saridakis, and C. Tzerefos, “Signatures of Superstring theory in NANOGrav,” [arXiv:2307.08601 \[hep-th\]](#).
- [71] J.-H. Jin, Z.-C. Chen, Z. Yi, Z.-Q. You, L. Liu, and Y. Wu, “Confronting sound speed resonance with pulsar timing arrays,” [arXiv:2307.08687 \[astro-ph.CO\]](#).
- [72] S. Balaji, G. Domènech, and G. Franciolini, “Scalar-induced gravitational wave interpretation of PTA data: the role of scalar fluctuation propagation speed,” [arXiv:2307.08552 \[gr-qc\]](#).
- [73] M. Bousder, A. Riadsolh, A. E. Fatimy, M. E. Belkacemi, and H. Ez-Zahraouy, “Implications of the NANOGrav results for primordial black holes and Hubble tension,” [arXiv:2307.10940 \[gr-qc\]](#).
- [74] Y. Li, C. Zhang, Z. Wang, M. Cui, Y.-L. S. Tsai, Q. Yuan, and Y.-Z. Fan, “Primordial magnetic field as a common solution of nanohertz gravitational waves and Hubble tension,” [arXiv:2306.17124 \[astro-ph.HE\]](#).
- [75] J. Yang, N. Xie, and F. P. Huang, “Nano-Hertz stochastic gravitational wave background as hints of ultralight axion particles,” [arXiv:2306.17113 \[hep-ph\]](#).
- [76] L. A. Anchordoqui, I. Antoniadis, and D. Lust, “Fuzzy Dark Matter, the Dark Dimension, and the Pulsar Timing Array Signal,” [arXiv:2307.01100 \[hep-ph\]](#).
- [77] R. A. Konoplya and A. Zhidenko, “Asymptotic tails of massive gravitons in light of pulsar timing array observations,” [arXiv:2307.01110 \[gr-qc\]](#).
- [78] M. Geller, S. Ghosh, S. Lu, and Y. Tsai, “Challenges in Interpreting the NANOGrav 15-Year Data Set as Early Universe Gravitational Waves Produced by ALP Induced Instability,” [arXiv:2307.03724 \[hep-ph\]](#).
- [79] G. B. Gelmini and J. Hyman, “Catastrogenesis with unstable ALPs as the origin of the NANOGrav 15 yr gravitational wave signal,” [arXiv:2307.07665 \[hep-ph\]](#).
- [80] H. Jiang, T. Liu, S. Sun, and Y. Wang, “Echoes of Inflationary First-Order Phase Transitions in the CMB,” *Phys. Lett. B* **765** (2017) 339–343, [arXiv:1512.07538 \[astro-ph.CO\]](#).
- [81] H. An, K.-F. Lyu, L.-T. Wang, and S. Zhou, “A unique gravitational wave signal from phase transition during inflation\*,” *Chin. Phys. C* **46** no. 10, (2022) 101001, [arXiv:2009.12381 \[astro-ph.CO\]](#).
- [82] H. An, K.-F. Lyu, L.-T. Wang, and S. Zhou, “Gravitational waves from an inflation triggered first-order phase transition,” *JHEP* **06** (2022) 050, [arXiv:2201.05171 \[astro-ph.CO\]](#).
- [83] D. Baumann, P. J. Steinhardt, K. Takahashi, and K. Ichiki, “Gravitational Wave Spectrum Induced by Primordial Scalar Perturbations,” *Phys. Rev. D* **76** (2007) 084019, [arXiv:hep-th/0703290](#).
- [84] K. Kohri and T. Terada, “Semianalytic calculation of gravitational wave spectrum nonlinearly induced from primordial curvature perturbations,” *Phys. Rev. D* **97** no. 12, (2018) 123532, [arXiv:1804.08577 \[gr-qc\]](#).

- [85] P. Adshead, K. D. Lozanov, and Z. J. Weiner, “Non-Gaussianity and the induced gravitational wave background,” *JCAP* **10** (2021) 080, [arXiv:2105.01659](#) [[astro-ph.CO](#)].
- [86] C. T. Byrnes, P. S. Cole, and S. P. Patil, “Steepest growth of the power spectrum and primordial black holes,” *JCAP* **06** (2019) 028, [arXiv:1811.11158](#) [[astro-ph.CO](#)].
- [87] S. R. Coleman, “The Fate of the False Vacuum. 1. Semiclassical Theory,” *Phys. Rev. D* **15** (1977) 2929–2936. [Erratum: *Phys.Rev.D* 16, 1248 (1977)].
- [88] C. G. Callan, Jr. and S. R. Coleman, “The Fate of the False Vacuum. 2. First Quantum Corrections,” *Phys. Rev. D* **16** (1977) 1762–1768.
- [89] E. Forest and R. D. Ruth, “Fourth-order symplectic integration,” *Physica D Nonlinear Phenomena* **43** no. 1, (May, 1990) 105–117.
- [90] H. Yoshida, “Construction of higher order symplectic integrators,” *Phys. Lett. A* **150** (1990) 262–268.
- [91] H. An and C. Yang, “Gravitational Waves Produced by Domain Walls During Inflation,” [arXiv:2304.02361](#) [[hep-ph](#)].